Electrochimica Acta 212 (2016) 701–709

Contents lists available at ScienceDirect

Electrochimica Acta

journal homepage: www.elsevier.com/locate/electacta

Tailoring three dimensional α–MnO_2/RuO_2 hybrid nanostructure as prospective bifunctional catalyst for Li–O_2 batteries

Hosaeng Jang[a], Awan Zahoor[c], Yongbin Kim[a], Maria Christy[b], Mi Young Oh[b], Vanchiappan Aravindan[d], Yun Sung Lee[e,*], Kee Suk Nahm[a,b,*]

[a] Department of Energy Storage and Conversion Engineering, Chonbuk National University, Jeonju 561–756, Republic of Korea
[b] R&D Education Centre for Fuel Cell Materials & Systems, Chonbuk National University, Jeonju 561–756, Republic of Korea
[c] Department of Chemical Engineering, N.E.D. University of Engineering & Technology, University Road Karachi, 75270, Pakistan
[d] Energy Research Institute @ NTU (ERI@N), Nanyang Technological University, Research Techno Plaza, 50 Nanyang Drive, 637553, Singapore
[e] Faculty of Applied Chemical Engineering, Chonnam National University, Gwangju 500–757, Republic of Korea

ARTICLE INFO

Article history:
Received 16 May 2016
Received in revised form 12 July 2016
Accepted 12 July 2016
Available online 14 July 2016

Keywords:
Lithium oxygen battery
electrocatalyst
hybrid materials
three dimensional nanostructures
α–MnO_2/RuO

ABSTRACT

We have synthesized three dimensional architectural α–MnO_2/RuO_2 hybrid nanostructures with three different compositions of (75:25), (69:31) and (50:50) by hydrothermal approach and evaluated their bifunctional electrocatalytic activity for Li–O_2 battery applications. The morphology of the α–MnO_2/RuO_2 nanostructures changed from sharp sea urchins to solid nanospheres with increasing RuO_2 content in the composition. The variations observed in physical, structural, morphological and electrochemical properties were characterized with respect to the MnO_2/RuO_2 concentrations by step by step analyses. MnO_2 exhibited better ORR catalytic activity, while RuO_2 revealed superior OER catalytic activity. Among the concentrations investigated, α–MnO_2:RuO_2 (75:25) exhibited superior catalytic activity for oxygen reduction and evolution reactions in aqueous media. This excellent catalytic activity logically led us to apply it as air-cathode catalyst in Li–O_2 cell, which produced a maximum capacity of >8100 mAh g^{-1} with high columbic efficiency and cyclability. The superior performance of the hybrid nanostructure is mainly attributed to its structural and compositional design which favors the electrochemical activity. Based on a careful investigation on the structural characterizations, the growth mechanism of the 3D nanostructured α–MnO_2/RuO_2 mixed oxides is discussed in detail.

1. Introduction

Li–O_2 batteries offer a dramatic increase in theoretical energy density relative to Li–ion cells, opening up the possibility for electric vehicle applications [1–4]. Li–air battery operates by means of electrochemical reactions that involve oxygen reduction reaction (ORR) during discharge and oxygen evolution reaction (OER) during recharge, utilizing the supplied oxygen on the cathode. However, the reverse process of charging requires a high potential to decompose the previously formed solid discharge products (Li_2O_2), which results in the disintegration of organic electrolytes and electrode materials [5,6]. Hence, unfortunately the complete conversion of solid discharge products, at low over-potential, remains a great challenge. Therefore, it is necessary to design and/or develop a promising bifunctional electrocatalyst to improve the reversibility of the Li–O_2 battery by improving the kinetics of ORR and OER, as well as lowering the overpotential [7]. The overall performance of the Li–O_2 battery itself depends primarily on the bifunctional electrocatalyst more than anything else.

In this regard, various bifunctional electrocatalysts have been explored as prospective candidates for Li–O_2 application, and so far Pt is considered to be the best ORR catalyst and Ru the best OER catalyst [8,9]. However, to reduce the cost and sustain the efficiency, recently, a greater focus had been aimed towards non–precious metal oxides and carbonaceous metal incorporated heteroatoms [10–12]. Particularly transition metal mixed oxides have been regarded as cost–effective catalysts for metal–air batteries. Among them, MnO_2 have been realized as a better replacement for noble metal Pt catalysts with superior ORR activity [12–15]. MnO_2 possess many advantages including high specific energy capacity, low cost and high material abundance in addition to being environmental friendly. On the other hand, due to the

* Corresponding authors.
E-mail addresses: leeys@chonnam.ac.kr (Y.S. Lee), nahmks@jbnu.ac.kr (K.S. Nahm).

http://dx.doi.org/10.1016/j.electacta.2016.07.067
0013-4686/

unique characteristics such as metallic conductivity, high chemical and thermal stability, catalytic activity and electrochemical redox properties, Ru and RuO_2 in both crystalline and amorphous forms are of practical importance as OER catalyst [16–18]. For example, Ru/C had exhibited high catalytic activity to oxidize Li_2O_2 in rechargeable lithium air battery compared to Pt/C and Au/C catalysts according to Harding et al. (2012) [16]. Sun et al. (2013) [17] also proved the Ru nanocrystals supported on carbon black as effective catalyst for the decomposition of discharge products (Li_2O_2). Meanwhile, Jung et al. (2012) [18] reported that ruthenium oxide (RuO_2) supported on graphene outperformed metallic ruthenium (Ru) supported on graphene by superior catalytic activity and remarkably reduced charge overpotential in Li–O_2 batteries. In that concept, therefore, MnO_2–RuO_2 mixed oxide would be the finest combination as bifunctional (ORR and OER) electrocatalyst. The advantage of mixed oxides is that they are known to have reasonable catalytic activity and structural stability as well as acceptable electronic properties [19,20].

The MnO_2–RuO_2 mixed oxides have been studied for electrochemical applications like supercapacitors to improve the rate capability and cycle performance [21–23]. Similarly, Guo et al. [19] investigated the electrochemical characterization of the nanosized Mn–Ru binary oxides as effective bifunctional cathode electrocatalysts for rechargeable Li–O_2 battery application. As reported by Guo et al. [19], the as–synthesized mixed oxides containing fusiform γ-MnO_2 nanorods and small RuO_2 nanoparticles exhibit remarkable electrocatalytic activities towards both ORR and OER. Li–O_2 batteries with Mn–Ru oxides catalyzed cathode delivered greater specific capacity than only Ketjen black (KB) cathode. In this trend, very recently Browne et al. (2016) [24] has published a highly active electrocatalysts based on Mn_3O_4/RuO_2 for OER activity in alkaline media and recorded low overpotential. According to the authors, regardless of the Mn:Ru ratio in the mixed oxides, a majority of the mixed Mn/Ru catalysts are highly active for OER, demonstrating that Mn/Ru mixed oxides are promising bifunctional catalysts to lower the charge overpotential and increase the discharge capacity of the batteries.

Morphology–controllable synthesis is necessary in the field of catalysis in order to develop the possibility of improving electrochemical properties by tailoring the morphology and surface structures in a nanoscale [25–27]. In particular, three dimensional (3D) nanostructures exhibit unique properties that make them better suitable as catalysts. Mainly the high surface area–to–volume ratios, and large directions for charge transport, diffusion of electrolytes and oxygen, makes 3D structures viable for catalysts. 3D structures could simultaneously construct smooth pathways for extremely rapid charge/discharge processes in addition to the electrons, electrolytes and oxygen during the process. Hence, we have attempted to develop a 3D bifunctional mixed oxide catalyst with morphology control to be applied as air cathode catalyst of Li–O_2 battery. In our previous work [20], three dimensional (3D) sea urchin shaped α–MnO_2/RuO_2 mixed oxides in a weight ratio of 82:18 was synthesized and examined as air cathode catalyst for ORR and OER in Li–air batteries. In the work, it was found that the 3D α–MnO_2/RuO_2 nanostructure is comparable to that of commercial Pt/C catalyst to catalyze ORR and OER with fast kinetics and without electrolyte decomposition.

In this work, we have attempted to optimize the mixed oxide catalyst composition and structure to achieve better electrocatalytic activity and stability in order to maximize the efficiency of Li–O_2 batteries. To establish the best combination of the as–prepared (α–MnO_2/RuO_2) hybrids, three different combination/ratios *viz.* (75:25), (69:31) and (50:50) have been synthesized and their physical and electrochemical properties have been comparatively studied in detail with respect to the previously reported (82:18). Using various analytic techniques, the variation in all the physical, structural, morphological and electrochemical properties were characterized with respect to the RuO_2 concentration (25 to 31 and 50 wt.%) or MnO_2 (75 to 69 and 50 wt.%). MnO_2 exhibited better ORR catalytic activity, while RuO_2 revealed superior OER catalytic activity. Among the various combinations, α–MnO_2/RuO_2 (75:25) hybrid exhibited superior ORR and OER activity and battery profiles. Further extensive structural, morphological and electrochemical studies were performed and discussed in detail to explain why (75:25) produced better electrocatalytic activity. Based on a careful investigation on the structural characterizations, the growth mechanism of the 3D nanostructure α-MnO_2/RuO_2 mixed oxides is also discussed in detail.

2. Experimental Methods

2.1. Synthesis of α–MnO_2/RuO_2 mixed oxides

α–MnO_2/RuO_2 mixed oxide materials were synthesized at different ratios *viz.* 75:25, 69:31 and 50:50 (by wt.%) by a conventional hydrothermal approach as reported in the previous article [20]. Analytical grade chemicals (Sigma–Aldrich) were used as the precursors for the preparation of hybrids without any further purification. Detailed descriptions of the synthetic process can be found in our previous report [20]. For the preparation of α–MnO_2/RuO_2 hybrids, 0.34 g $MnSO_4.H_2O$, 0.54 g of $K_2S_2O_8$, 2 mL of H_2SO_4 and appropriate amount of $RuCl_2.H_2O$ were added into 40 ml deionized water and stirred continuously for 30 min. The amount of $RuCl_2.H_2O$ varied according to the composition such as 0.119, 0.016 and 0.35 for (75:25), (69:31) and (50:50), respectively. Then, the mixed solution was transferred in to a Teflon lined stainless steel autoclave and kept at 110 °C for 6 h. The autoclave was then cooled down to room temperature and the resultant product was harvested. The final product was centrifuged and washed several times with deionized water and dried at 60 °C for 8 h to yield the hybrids.

2.2. Characterizations

Powder X–ray diffraction (XRD, Shimadzu XRD–6000 with CuKα radiation (λ = 1.54 Å)) analysis were performed to study the structural properties. The morphological properties were examined with field emission scanning electron microscopy (FESEM, JSM–6700F), high resolution transmission electron microscopy (HR–TEM, JEM–2010, JEOL) and corrected scanning transmission electron microscopy (CS–TEM, JEM–ARM200F, JEOL). Chemical compositions of the samples were investigated with inductively coupled plasma mass spectrometer (ICP–MS, Agilent 7500a, Agilent Technologies), X–ray photoelectron spectroscopy (XPS, Thermo scientific Kα X–ray source), and energy dispersive X–ray spectroscopy (EDX). The Brunauer–Emmett–Teller (BET) specific surface area measurements were conducted using BELSORP, Japan.

Electrocatalytic activity of the sample was evaluated by measuring ORR and OER polarization curves. The electrochemical studies were carried out using a computer controlled potentiostat (CHI 760D, CH Instrument) equipped with a typical three electrode cell. The details of electrochemical characterizations and Li–air battery fabrication are included in the supplementary article.

3. Results and discussion

3.1. Crystal structure

The crystal structure of the synthesized hybrid metal oxides was analyzed by XRD measurements and the results are shown in Fig. 1. From Fig. 1, it could be seen that all the observed XRD peaks are well indexed to tetragonal α–MnO_2 with I_4/m space group and

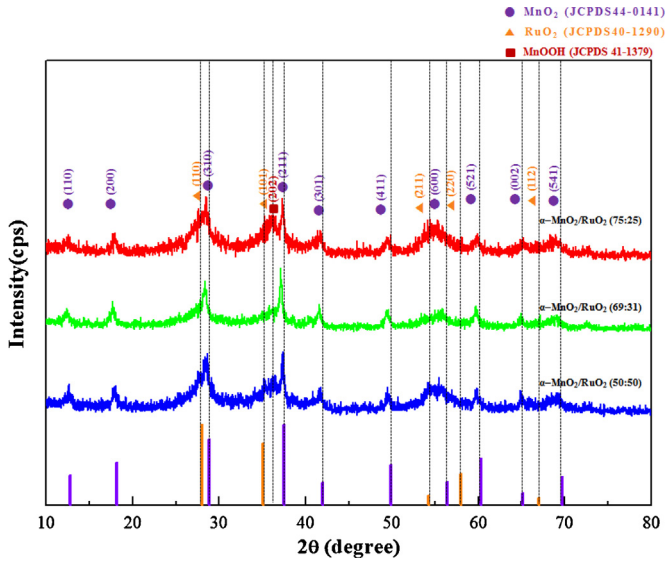

Fig. 1. X–ray diffraction patterns of α–MnO_2/RuO_2 hybrids synthesized in three different ratios.

tetragonal RuO_2 with $P4_2/mnm$ space group which confirms the formation of α–MnO_2/RuO_2. The lattice constants of α–MnO_2 and RuO_2 were calculated from the XRD pattern using Rietveld method [20]. The peaks and values are in very good agreement with the literature values (JCPDS 44–0141 and JCPDS 40–1290). Nonetheless, the presence of MnOOH, (an intermediate of MnO_x [28]), could be traced from the peak at about 2θ = 36° of the patterns [JCPDS 41–1379]. The relative peak intensity of α–MnO_2 is higher than that of RuO_2, indicating better crystallinity for MnO_2 compared to RuO_2. Similar XRD patterns were observed by Guo et al. [19] and Browne et al. [24] for Mn–Ru based mixed oxides.

XPS analysis and ICP–MS were performed to examine the elemental compositions of the prepared α–MnO_2/RuO_2 hybrids and the results are given in the supplementary article as Fig. S1 and Table S1, respectively. The XPS survey of all the hybrids (75:25), (69:31), and (50:50) revealed the existence of Mn, Ru and O in the nanostructures (Fig. S1 (a)). Also, the theoretically calculated stoichiometric weight percent values of Mn, Ru and O, matched with the experimentally measured ICP–MS values (Table S1, supplementary article).

3.2. Morphological properties

Fig. 2 presents the morphology of three different α–MnO_2/RuO_2 hybrids (75:25), (69:31) and (50:50). For comparison, native α–MnO_2 and RuO_2 prepared under same experimental conditions are included in Fig. 2. The α–MnO_2 exhibits urchin shaped nanostructures (comprised of nanoneedles) with an average size of 2.5–3.0 μm. A similar morphology is retained upon incorporation of RuO_2 at different concentrations (25 and 31 wt.%). At 50 wt.%, however, the urchin shape has been completely vanished and a spherical morphology is observed which is similar to that of the native RuO_2. Apparently, negligible amount of deviation in the size of the urchins are noted, but obvious variation is realized for the thickness of the needles. Particularly, increase in the needle thickness is evident with increase in RuO_2 concentration in the hybrid. The average particle size and needle thickness of the mixed oxides are summarized along with the surface area properties in Table S2 of the supplementary article.

In order to understand the morphological development and structural changes in the α–MnO_2/RuO_2 hybrids, HR–TEM analysis was performed as given in Fig. 3. The HR–TEM image of the α–MnO_2/RuO_2 (75:25) reveals urchin structure with prominent nanoneedles structures and uniform one dimensional growth. In the previously reported composition (82:18), single nanoneedle of α–MnO_2/RuO_2 (82:18) urchin structure exhibited sharp and thin needle structures without prominent outline and homogeneous distribution of RuO_2 [20]. Compared to the 82:18, increase in the amount of RuO_2 (25%) can be clearly noticed in Fig. 3 (b) with high particle concentration near the outline of the nanoneedles. The interplanar distances marked in the lattice planes in Fig. 3a, well coincide with the distance of (220) and (110) planes of MnO_2, which is consistent with the XRD observations. Also, the crystallinity is evident from SAED pattern in Fig. 3a and similar observation was also made in Fig. 3b. The needle outer line continues to grow thicker and shorter as the RuO_2 content is further increased to 31 wt.% (Fig. 3b). This certainly makes the needle structure appear shorter in length and hollow in the middle with thicker outline (Fig. 3b, inset), which is consistent with earlier FE–SEM observations. At 50 wt.% of RuO_2, the nanoneedles

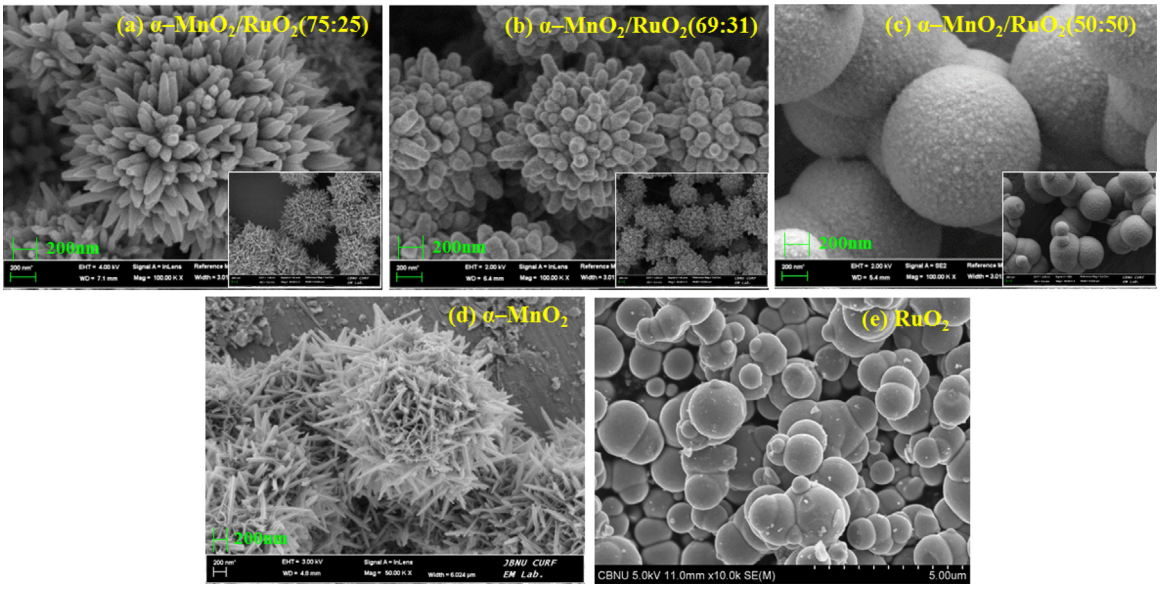

Fig. 2. FESEM images of α–MnO_2/RuO_2 hybrids at (a) (75:25), (b) (69:31) and (c) (50:50) ratios, and (d) α–MnO_2 and (e) RuO_2.

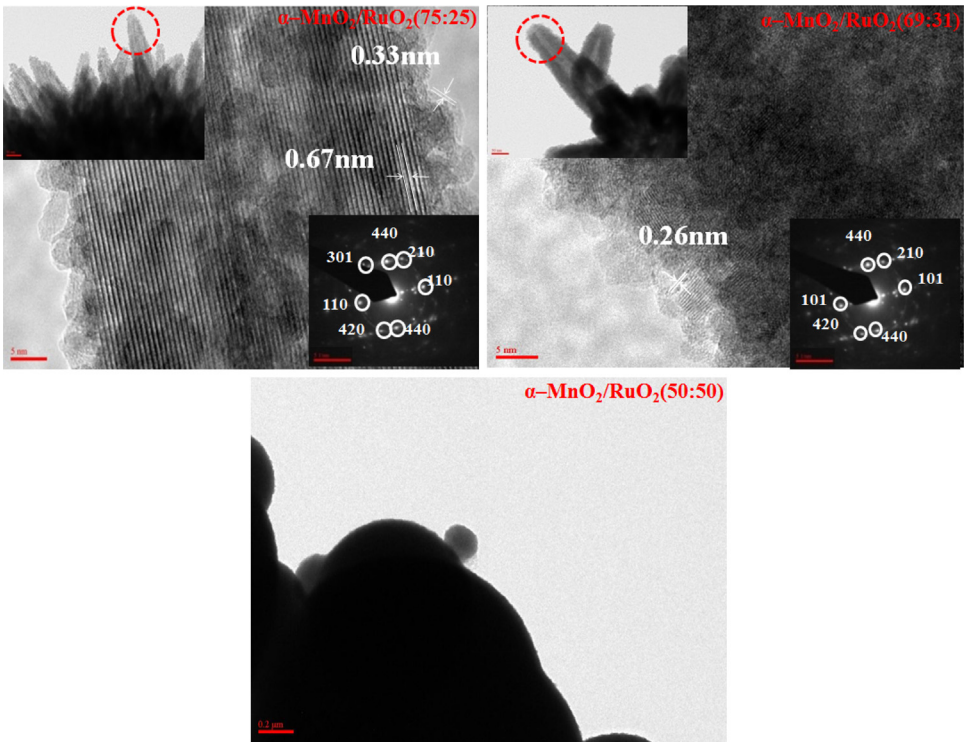

Fig. 3. HRTEM images of α–MnO_2/RuO_2 hybrids at three different ratios.

completely disappear resulting in the formation of spheres. Since the material surface was thicker, it is not possible to study the interior morphology of (50:50) structure by HR–TEM (Fig. 3c). However, both FE–SEM and TEM observations clearly support each other in terms of the structural transformation from urchin structures to spheres.

The presence and distribution of elements like Mn, Ru and O at three different proportions (75:25), (69:31), and (50:50) were also verified by SEM–EDX analysis and are given in Fig. S2 (supplementary article). Specific properties such as surface area measurements, corresponding N_2 adsorption–desorption isotherms and pore size distribution were also analyzed and included in supplementary article as Fig. S3.

4. Growth mechanism of nanostructures

The properties of a metal oxide nanostructure are determined by various physicochemical parameters which include their size, shape, composition, and structure [26]. By controlling each of these parameters the properties of metal oxide nanostructures can be easily tailored and calibrated. Hence, it is crucial to understand the growth behavior and evolution of morphology for efficient synthesis and control of nanostructures. The formation of α–-MnO_2/RuO_2 hybrids could be expressed through the following reaction equation [19,20]

$$MnO_4^- + 3Ru^{3+} + 4H_2O \leftrightarrow MnO_2 + 3RuO_2 + 8H^+ \quad (2)$$

while, the formation of α–MnO_2 could be expressed as follows [29],

$$4MnO_4^- + 4H^+ \rightarrow 4MnO_2(S) + 2H_2O + 3O_2 \quad (3)$$

Similarly the formation mechanism of RuO_2 could be expressed as follows,

$$Ru^{3+} + 3H_2O \rightarrow Ru(OH)_3 + 3H^+ \quad (4)$$

$$4Ru(OH)_3 + O_2 \rightarrow 4RuO_2 + 6H_2O \quad (5)$$

In this work, the α–MnO_2/RuO_2 hybrids were synthesized at 110 °C for six hours. Generally both temperature and reaction time could similarly influence the morphology of the synthesized nanostructures. From the structural perspective, the morphology of the mixed oxides seems to have been influenced by the reaction rate of the precursor materials which vary according to the proportion of the mixed oxides. The formation of the intrinsic anisotropic nanocrystals is found to be a highly kinetically driven process. Such processes occur far from the thermodynamic equilibrium and are overdriven by high precursor concentrations [30]. We believe that the formation MnO_2 nanourchin structures can be rationally expressed as a kinetically–controlled, dissolution–recrystallization mechanism. The formation mechanism of urchin shaped α–MnO_2 could be explained as follows: initially, the high precursor concentration leads to the rapid formation of a large number of nuclei, followed by slow crystal growth. At first, MnO_2 colloids are produced and aggregated to form microspheres which become nanoparticles. Then, the MnO_x crystals condense into two–dimensional sheets during the reduction of $KMnO_4$. Thus formed sheets curl into smaller nanorods in the presence of K^+ ions at elevated temperature and pressure under hydrothermal conditions [30]. Smaller nanorods subsequently grow to larger ones *via* Ostwald ripening process [31]. Clearly, the crystallites have high surface energy in the inner cores than outer surfaces and thus could be easily dissolved which must be the reason for the formation of wider and longer nanorods. According to Wang et al. [32] the reactant concentration yield different effects on the formation rate of different crystal faces, which could be applied towards the preparation of nanostructures. It is also noteworthy that α–MnO_2 have the growth habit of forming one–dimensional nanorods at suitable environments [29]. Thus one–dimensional α–MnO_2 nanorods are initially formed along [001] facets from the colloidal microspheres. They become energetically stable by experiencing oriented attachment resulting in the self–assembly of nanourchin structures. Thus epitaxial

growth of nanorods along the surface of initial microspheres and formation of solid urchin structures takes place.

On the other hand, formation of RuO_2 could be explained by thermodynamically stable process. Here again the growth process of nuclei could be described by the Ostwald ripening mechanism, in which the growth of larger particles occur at the expense of smaller ones driven by surface energy reductions [31]. In detail, the interfacial energy is the energy associated with an interface owing to the difference between the chemical potential of atoms in an interfacial region and the atoms in neighboring bulk phases. Differences in the local equilibrium concentrations set up concentration gradients and provide the driving force for the growth of larger particles at the expense of smaller particles. This phenomenon has been extensively used to explain the formation of thermodynamically stable nanocrystals with nearly spherical morphologies. The formation of spherical shaped RuO_2 nanocrystals could also be explained in the same manner (Fig. 2 (f)). The ruthenium precursors are rapidly precipitated to form $RuO_2{\cdot}xH_2O$ particulates during the initial period of the hydrothermal synthesis. Meanwhile, the condensation of hydroxyl groups and growth of RuO_2 crystallites occur sequentially, which could be reasonably attributed to the hydrothermal reaction time. The crystal size of RuO_2 could be easily controlled by varying the reaction time [33].

In the case of mixed oxide, there are two main points to be considered. First, when the single crystal structure of the seed is fixed, the final shape of the nanocrystal depends on the relative growth rate of both crystallographic planes. Second, the facets with slower growth rate will be expressed more on the surface which results in the formation of different nanostructures as inferred from Figs. 2, 3 and S2 (supplementary) [34]. In that case 1D MnO_2 nanorods were initially formed along [001] facets due to the high concentration, while ruthenium precursors were rapidly precipitated to form $RuO_2{\cdot}xH_2O$ particulates during the initial period of hydrothermal synthesis followed by sequential crystal growth all over the nanostructure. The final structure and shape varied

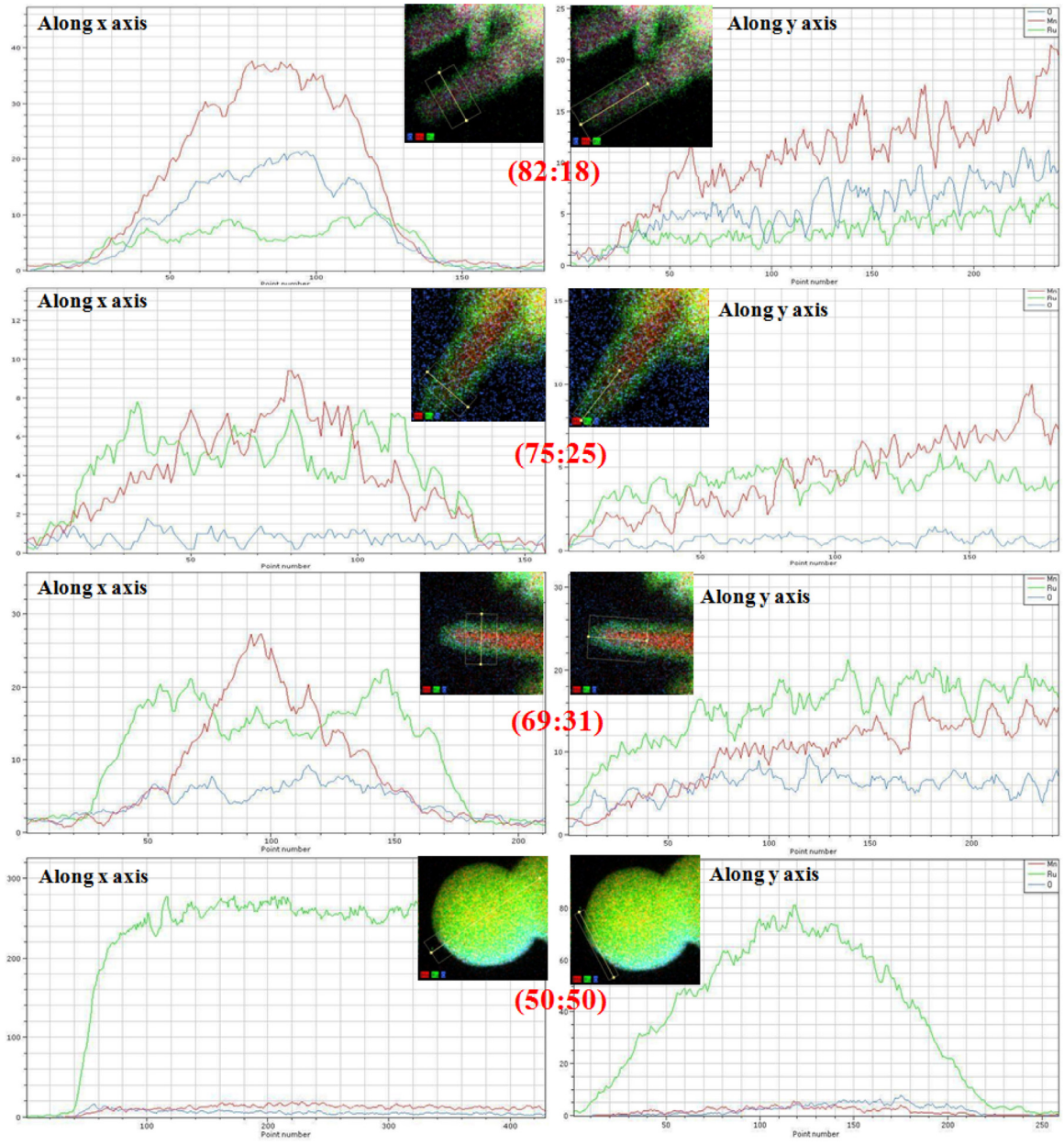

Fig. 4. Cs–corrected TEM (a) images and (b) mapping of α–MnO_2/RuO_2 hybrids (82:18) (75:25), (69:31) and (50:50).

between nanourchins to nanospheres owing to the relative growth rates of the mixed oxides.

For a deeper understanding, the growth mechanism of the synthesized mixed oxides was analyzed with respect to the previously reported (82:18) concentration [20]. In the case of 18 wt.% RuO_2 loading, MnO_2 nucleus must have got fixed first, acting as the skeleton so that the resulting mixed oxide grows into the urchin shape of MnO_2. This is most likely due to the high concentration of MnO_2 precursors resulting in a relatively high crystal growth rate. As a result, RuO_2 is mostly expressed on the surface of the nanostructure owing to its slow growth rate. The formation of urchin shaped MnO_2 by rapid formation of large number of nuclei followed by the slower crystal growth. So, in this case, as the proportion of RuO_2 increased (25 wt.%), the crystal structure of mixed oxides has slowly transformed. The morphology was observed to change dramatically from sharp and thin nanourchin structures to blunt and thick structure which could be ascribed to the dissolution and re–crystallization effect under the high reaction temperature and pressure. As the RuO_2 content increased more (31 wt.%), the nanoneedles grew shorter and thicker which is clearly inferred from Fig. 2. Interestingly, the hybrids with equal concentration (50 wt.%) exhibit spherical shaped morphology similar to that of native RuO_2. With equal proportion, the formation of MnO_2 and RuO_2 seems to compete with each other and the MnO_2 urchin structures are completely suppressed by the formation of spherical structures. Thus, the nanourchins with short and thick nanoneedles are completely dominated with RuO_2 resulting in spherical structures. Further, smooth and completely covered RuO_2 structures exhibit core–shell morphology with MnO_2 core evident from Figs. 3 and S2.

Crystallographic and morphological analyses clearly parallel the above predictions and helps to understand the formation mechanism. In an advanced level of investigation, CS corrected TEM was also utilized to validate the growth mechanism in an atomic scale. The growth mechanism can be perceived in a better way with the linear mapping of the cross section in CS–TEM. The CS–TEM mapping images show the detailed view of the tip of nanoneedle of the synthesized hybrids. The linear mappings along both X and Y axes of the CS of nanoneedles are marked as shown in Fig. 4. For a clear picture, the mapping of (82:18) was also performed and the growth was analyzed systematically for (82:18), (75:25), (69:31), and (50:50). Fig. 4 is similar to that of EDX mapping and shows almost even distribution of Mn, Ru and O for 18 wt.% loading of RuO_2. Nevertheless, a thin RuO_2 rich wall can be observed at this concentration. To explore this, corresponding linear mapping of the cross section of the same part of the nanoneedle along X axis is observed which confirms the Mn rich peak on the inside and uniform distribution of RuO_2 throughout the needle. Along the Y axis, *i.e.* along the needle structure, the mapping shows rich Mn content followed by O and Ru. The Mn rich observation is mainly because the mixed oxide contains 82% of MnO_2. Similarly the CS–TEM mapping of α–MnO_2/RuO_2 hybrids with higher loading of RuO_2 (25 and 31 wt.%) were recorded and corresponding CS linear mapping is given in Fig. 4 as well. Increasing the loading clearly shows distinct outline wall and the hollow interior. Obviously, homogeneous distribution of O is evident across the nanoneedle structures. As expected, the absence of needle structure is noted for 50 wt.% RuO_2 loading (Fig. 4), and hollow core–shell structure with Mn core and Ru shell with evenly distributed O is observed. The linear mapping along the X and Y axes shows only the Ru content since RuO_2 covers the presence of MnO_2 present in the core (Fig. S2 (supplementary)). This gives a clear understanding on the growth and structural characteristics of our synthesized α-MnO_2/RuO_2 mixed oxides.

The mixed oxide with the highest MnO_2 content (82:18) is just native α–MnO_2 itself with regard to its morphology and structural characteristics. The (50:50) mixed oxide exhibited a different nanostructure than that of the other three ratios, forming just nanospheres similar to native RuO_2. In between, the (75:25) and (69:31) mixed oxides exhibit slightly modified nano-urchin structures with Mn content comparatively higher than Ru. From the EDX (Fig. S2), and Cs–TEM mapping (Fig. 4), it is clear that the structural characteristics gradually lean towards RuO_2 structures as the ratio of RuO_2 slowly increased within the mixed oxide.

5. Electrochemical characteristics

The electrocatalytic activity (ORR and OER) of the synthesized mixed oxide catalysts in aqueous media were qualitatively estimated from the reduction and oxidation peak potentials, respectively, from CV and LSV curves. The CV and LSV analyses are produced in detail in the supplementary article, Fig. S4 (a–d).

5.1. Electrochemical characteristics in non-aqueous medium

Similar to the electrocatalytic activity of α–MnO_2/RuO_2 in aqueous media, CV was also analysed in organic medium (1 M LiTFSI in TEGDME). For this analysis, the best performing composition (α–MnO_2/RuO_2 (75:25)) in aqueous medium was selectively evaluated along with KB and commercial Pt/C for comparative analysis. The CV curves of all the cells were recorded in the range of 1.5 to 4.7 V *vs.* Li at a scan rate of 0.01 mV s^{-1} as given in Fig. 5. It could be seen that all the electrodes KB, Pt/C and α–MnO_2/RuO_2 (75:25) exhibit a clear reduction peak at 2.52, 2.54 and 2.53 V *vs.* Li, respectively. This prominent reduction peak at 2.53 V *vs.* Li indicates the reduction reaction of oxygen *i.e.* $2Li^+ + O_2 \rightarrow 2e^- + Li_2O_2$

During oxidation, a prominent and high intensity peak at 4.26 V *vs.* Li was noted for α–MnO_2/RuO_2 followed by Pt/C at 4.33 V *vs.* Li whereas KB showed a very poor and broad oxidation peak at 4.54 V *vs.* Li. On close observation, appearance of tiny peak at 3.4 V *vs.* Li could be seen for all the three electrodes which could be attributed to the oxidation of LiO_2 formed upon chemical reduction of Li and O_2 during Li_2O_2 formation [36,37]. This is another reason why the

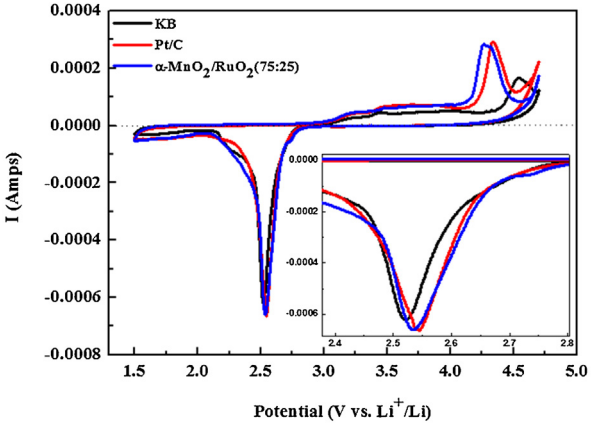

Table 1

	Reduction reaction		Oxidation reaction	
	Peak Potential (V)	Peak Current (mA)	Peak Potential (V)	Peak Current (mA)
KB	2.52	-6.23	4.54	1.66
Pt/C	2.54	-6.65	4.33	2.93
α-MnO_2/RuO_2(75:25)	2.53	-6.60	4.26	2.85

Fig. 5. CV curves of α–MnO_2/RuO_2 (75:25) analyzed in organic medium (1 M LiTFSI in TEGDME) recorded in the range of 1.5 to 4.7 V *vs.* Li at a scan rate of 0.01 mV s^{-1}. Inset Table 1 summarizes the peak potential and peak currents for CV curves analyzed in organic medium.

peak current for reduction reaction is higher than the evolution reaction. The peaks at 3.4 V *vs.* Li are thin and week which show that the reaction kinetics were rapid at this conversion. From these results it is conclusive that α–MnO_2/RuO_2 is effective for both ORR and OER reaction in organic medium with less polarization. There are no other peaks found during the ORR and OER reactions demonstrating a proper reduction and evolution of oxygen or a one–step reversible reaction. Comparing the result with that of CV obtained in aqueous media Fig. S4 (a), it could be seen that both the results are consistent with each other showing positively shifted onset potentials and high peak current for α–MnO_2/RuO_2 (75:25). This shows that the CV traces obtained in aqueous media is as reliable as the one obtained in non–aqueous system. From both studies, it is well established that α–MnO_2/RuO_2 (75:25) could be a suitable and efficient bifunctional catalyst applicable for Li–O_2 battery air cathode.

5.2. Li–O_2 battery application

To evaluate the electrocatalytic activity of α–MnO_2/RuO_2 hybrid nanostructures in Li–O_2 battery, all the nanostructures were employed as air cathode catalysts in aforementioned configuration. Accordingly, Li–O_2 cell was constructed using α–MnO_2/RuO_2 hybrids as catalysts in TEGDME based electrolyte in a Swagelok™ type cell. Fig. 6 (a) shows the typical charge–discharge traces of Li–O_2 cell tested at a current density of 0.1 mA cm^{-2}. Obviously, the air cathodes prepared with all the synthesized α–MnO_2/RuO_2 hybrids catalysts exhibit high discharge capacities with good reversibility. For example, first discharge capacities of 8250, 6150 and 4650 mAh g^{-1} were noted for (75:25), (69:31) and (50:50), respectively. This certainly proves that α–MnO_2/RuO_2 (75:25) is the most efficient catalyst compared to other investigated catalysts. The obtained results, especially with the well performing α–MnO_2/RuO_2 (75:25) catalyst (8250 mAh g^{-1}) is much better than the previously reported discharge capacity of 6500 mAh g^{-1} with 45 wt.% Mn–Ru mixed oxides measured in $LiCF_3SO_3$ (TEGDME) medium [19]. Also, from Fig. 6 (a) the overpotential of α–MnO_2/RuO_2 (75:25) catalyzed cell is found to be 0.7 V which is better than all other compositions. The reduced overpotential surpassed the previously reported Mn-Ru binary oxides [19] and our previous study [20] indicating that (75:25) could be the optimum composition for α–MnO_2/RuO_2 mixed oxides to deliver better bifunctional activity. However, recent report [18] with ruthenium oxide (RuO_2) supported on graphene outperformed MnO_2/RuO_2 composites owing to the high surface area carbon support. So the performance of MnO_2/RuO_2 could still be improved with carbon supports like graphene which would lead the present work in to another direction. Fig. 6 (b) represents the cycling profiles of Li–O_2 cells for about 5 cycles. Among the synthesized compositions, α–MnO_2/RuO_2 (75:25) displayed overall superior battery performance with less over potential, high capacity and reversibility which is consistent with the earlier OER and ORR results.

To prolong the cycleability and reversibility of Li–O_2 cell, the capacity has been limited to 1000 mAh g^{-1} and tested for cyclability. Fig. 6 (c) and (d) shows the cycling performance of α–MnO_2/RuO_2 nanostructures catalyzed Li–O_2 batteries tested at a constant current density of 0.1 mA cm^{-2} with limited depth of discharge and charge. Apparently, α–MnO_2/RuO_2 (75:25) nanostructure catalyzed cell delivers a stable cycling behaviour up to 44

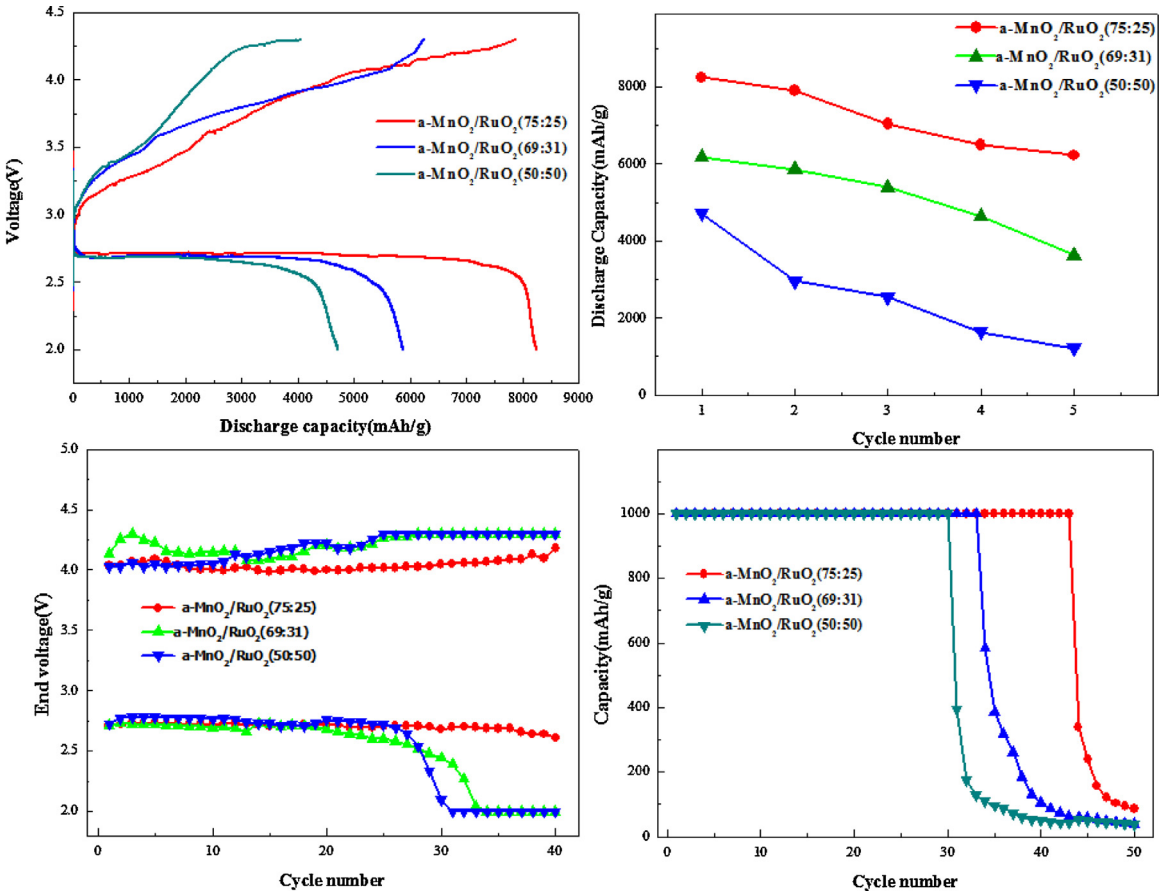

Fig. 6. (a) The first cycle charge–discharge capacities, (b) cycling profiles of α–MnO_2/RuO_2 hybrids catalyzed Li–O_2 battery measured at 0.1 mA cm^{-2}, (c) Charge–discharge potentials as a function of cycle number and (d) limited capacity cycling as a function of cycle number.

cycles. Nevertheless, inferior yet decent cycleability was noted for the rest of the compositions investigated. For example, α–MnO_2/RuO_2 (69:31) is stable up to 33 cycles and fades rapidly upon further cycling (Fig. 6 (c and d)).

The α–MnO_2/RuO_2 hybrids catalyzed Li–O_2 cells exhibit high capacities regardless of their structure or morphology. The combined feature and synergistic effect of individual oxides (α–MnO_2 being an excellent ORR and RuO_2 an OER catalysts) in the hybrid structure exhibit remarkable bifunctional activity upon cycling [12,18,19,20]. The superior electrocatalytic behaviour of α–MnO_2/RuO_2 toward ORR and OER afforded by its inherent electronic structure with favourable electronic transport capability is coupled with the 3D structure for excellent results. 3D structure not only provides more electrocatalytic sites but also promotes mass transport in the electrolyte [20]. The bifunctional catalysts certainly help with the proper formation and decomposition of reaction products which enabled the excellent reversibility of the cells. In particular, (75:25) hybrid structure possess maximum pore diameter of >10 nm and appreciable specific surface area (Table S2, supplementary) which is ideal condition to enhance the reversible reaction in Li–O_2 cell since the oxygen electrode could facilitate the accommodation and transportation of Li^+ ions and O_2. On the other hand, the pore properties could also be the reason for the capacity degradation upon extended cycling. Because, the solid discharge products formed upon forward reaction might accumulate deep inside the pores and does not undergo complete decomposition on reverse reaction. These pores might slowly get clogged in the process and the surface became inactive upon cycling which affect the cell performance [35]. Yet, this is not the entire reason behind the cell degradation upon cycling because bifunctional hybrids are used to promote the formation and decomposition reaction. Therefore, it is necessary to study post characterization if there were any unwanted products (other than Li_2O_2) formed over the surface owing to undesired decomposition/reaction which could impede the cell efficiency. So post-mortem studies were conducted on the α–MnO_2/RuO_2 (75:25) electrodes.

5.3. Post Characterization of Li–O_2 battery electrodes

To understand the reason behind the improved performance of the (75:25) catalyzed Li–O_2 cell compared to other ratios, post–mortem studies were conducted. After the preparation of the air cathodes with α–MnO_2/RuO_2 (75:25) catalyst, they were analysed freshly, and then, after separately discharging and charging with metallic Li (Fig. 7 (a)). The pristine electrode shows peaks for hybrids that vanished after first discharge *i.e.* upon Li_2O_2 formation. This means that, the intensity of the products observed in first discharge offsets the presence of the catalyst. Upon charge process, the discharge products, Li_2O_2, decomposes and hybrid peaks re–appears. Further, it is noted that there is no end product other than Li_2O_2 in the first discharge. Nevertheless, a trace amount of LiOH is observed because of the reaction between Li_2O_2 and structural water content in Mn–Ru oxides [20]. Fig. 7 (b) shows the FE–SEM images of pristine electrode examined before testing and, after first discharging and first charging, respectively. From the images it could be noticed that the surface of the pristine electrode was smooth with uniform porosity, and the discharge products are highly agglomerated on the surface of the cathode after discharging. The presence of discharge product Li_2O_2 is clearly supported from the XRD investigations. After charging, the electrode surface is almost reverted back to the original pristine electrode surface. According to Laoire et al. [36,37] Li_2O_2 formed with ether based electrolytes sometimes reduces to Li_2O before decomposing into Li and O_2. Thus formed Li_2O cannot be decomposed which could precipitate and block the pores on the

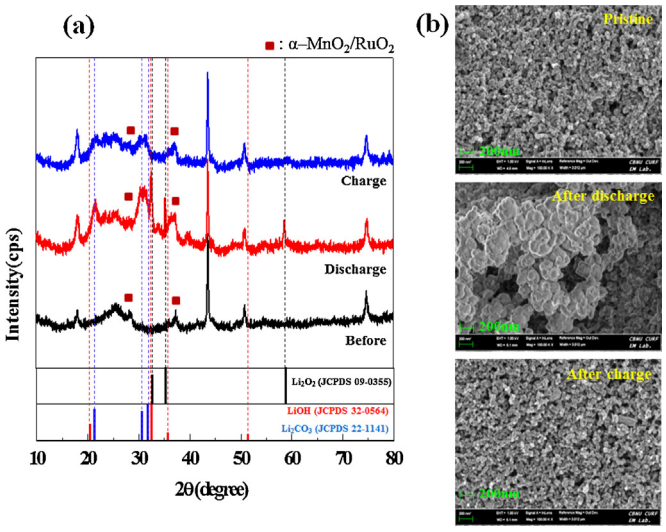

Fig. 7. (a) XRD patterns and (b) SEM images of α–MnO_2/RuO_2 hybrids catalyzed air cathodes measured (i) pristine, (ii) after discharge and (iii) after charge.

electrode surface resulting in an electrochemically inactive electrode. This phenomenon also accounts to the fade in capacity upon cycling. However, no such precipitation is observed for α–MnO_2/RuO_2 catalysts from the *ex–situ* FESEM and XRD investigations. After charging, the electrode surface is as smooth and porous as the original surface observed before cycling. Hence, the proper formation and decomposition of discharge product (Li_2O_2) could be evidenced that attests to the better performance of α–MnO_2/RuO_2 (75:25) catalyzed Li–O_2 cell.

6. Conclusions

A suitable mixed oxide bifunctional catalyst, α–MnO_2/RuO_2 with three dimensional nanostructures had been designed and optimized for Li–O_2 battery application. The increased RuO_2 content in the composition certainly influenced the morphological variation from sharp nanourchin to solid nanospheres. ORR and OER measurements revealed that MnO_2 acted as a promising ORR catalyst, and that the inclusion of RuO_2 significantly improved the OER performance. Among the compositions investigated, α–MnO_2/RuO_2 (75:25) exhibited the best electrocatalytic activity which is comparable to that of commercial Pt/C for ORR and even better than that of commercial RuO_2 for OER. The same behavior was confirmed in the organic solutions as well. The results indicated that the mixed oxides could be employed as suitable bifunctional catalysts for Li–air battery application. When employed as air cathode catalyst, α–MnO_2/RuO_2 (75:25) outperformed all other compositions in terms of specific capacity, capacity retention and efficiency. Thus α–MnO_2/RuO_2 could be employed as promising catalyst for Li–O_2 battery application considering the cost and eco–friendliness.

Acknowledgements

This work was supported by the Human Resources Development program (No.20114030200060) of the Korea Institute of Energy Technology Evaluation and Planning (KETEP) grant funded by the Korea government Ministry of Trade, Industry and Energy. This research was also supported by Basic Science Research Program through National Research Foundation of Korea (NRF) funded by the Ministry of Education (2009-0094031).

Appendix A. Supplementary data

Supplementary data associated with this article can be found, in the online version, at http://dx.doi.org/10.1016/j.electacta.2016.07.067.

References

[1] P.G. BrucePeter, S.A. Freunberger, L.J. Hardwick, J.M. Tarascon, Nat. Mater. 11 (2012) 19–29.
[2] H.G. Jung, J. Hassoun, J.B. Park, Y.K. Sun, B. Scrosati, Nat. Chem. 4 (2012) 579–585.
[3] G. Girishkumar, B. McCloskey, A.C. Luntz, S. Swanson, W. Wilcke, J. Phys. Chem. Lett. 1 (2010) 2193–2203.
[4] K.M. Abraham, Z. Jiang, J. Electrochem. Soc. 143 (1996) 1–5.
[5] Y.C. Lu, H.A. Gasteiger, M.C. Parent, V. Chiloyan, Y. Shao-Horn, Electrochem. and Sol. St. Lett. 13 (2010) A69–A72.
[6] A. Débart, J. Bao, G. Armstrong, P.G. Bruce, J. Power Sources 174 (2007) 1177–1182.
[7] L. Jörissen, J. Power Sources 155 (2006) 23–32.
[8] Y.C. Lu, Z. Xu, H.A. Gasteiger, S. Chen, K. Hamad-Schifferli, Y. Shao-Horn, J. Am. Chem. Soc. 132 (2010) 12170–12171.
[9] Y.C. Lu, H.A. Gasteiger, Y. Shao-Horn, J. Am. Chem. Soc. 133 (2011) 19048–19051.
[10] R. Cao, J.S. Lee, M. Liu, J. Cho, Adv. Energy Mater. 2 (2012) 816–829.
[11] Y. Zheng, Y. Jiao, J. Chen, J. Liu, J. Liang, A. Du, W. Zhang, Z. Zhu, S.C. Smith, M. Jaroniec, G.Q. Lu, S.H. Qiao, J. Am. Chem. Soc. 133 (2011) 20116–20119.
[12] A. Débart, A.J. Paterson, J. Bao, P.G. Bruce, Angew. Chem. Int. Ed. 47 (2008) 4521–4524.
[13] A. Zahoor, H.S. Jang, J.S. Jeong, M. Christy, Y.J. Hwang, K.S. Nahm, RSC Advances 4 (2014) 8973–8977.
[14] Y.L. Cao, H.X. Yang, X.P. Ai, L.F. Xiao, J. Electroanal. Chem. 557 (2003) 127–134.
[15] E.M. Benbow, S.P. Kelly, L. Zhao, J.W. Reutenauer, S.L. Suib, J. Phys. Chem. C 115 (2011) 22009–22017.
[16] J.R. Harding, Y.C. Lu, Y. Tsukada, Y.S. Horn, Phys. Chem. Chem. Phys. 14 (2012) 10540–10546.
[17] B. Sun, P. Munroe, G. Wang, Scientific Reports 3 (2013) 2247, doi:http://dx.doi.org/10.1038/srep02247.
[18] H.G. Jung, Y.S. Jeong, J.B. Park, Y.K. Sun, B. Scrosati, Y.J. Lee, ACS Nano 7 (4) (2013) 3532–3539.
[19] K. Guo, Y. Li, J. Yang, Z. Zou, X. Xue, X. Li, H. Yang, J. Mater. Chem. A 2 (2014) 1509–1514.
[20] H.S. Jang, A. Zahoor, J.S. Jeon, P. Kim, Y.S. Lee, K.S. Nahm, J. Electrochem. Soc. 162 (2015) A300–A307.
[21] T.S. Hyun, J.E. Kang, H.G. Kim, J.M. Hong, I.D. Kim, Electrochem. Solid-State Lett. 12 (2009) A225–A228.
[22] D.Y. Youn, H.L. Tuller, T.S. Hyun, D.K. Choi, I.D. Kim, Electrochem. Soc. 158 (8) (2011) A970–A975.
[23] J.C. Chou, Y.L. Chen, M.H. Yang, Y.Z. Chen, C.C. Lai, H.T. Chiu, C.Y. Lee, Y.L. Chueh, J.Y. Gan, J. Mater. Chem. A 1 (2013) 8753–8758.
[24] M.P. Browne, H. Nolan, G.S. Duesberg, P.E. Colavita, M.E.G. Lyons, ACS Catal. 6 (2016) 2408–2415.
[25] F. Cheng, J. Zhao, W. Song, C. Li, H. Ma, J. Chen, P. Shen, Inorganic Chemistry 45 (2006) 2038–2044.
[26] Y. Xia, Y. Xiong, B. Lim, S.E. Skrabalak, Angew. Chem. Int. Ed. 48 (2009) 60–103.
[27] K. Song, D.A. Agyeman, J. Jung, M.R. Jo, J. Yang, Y.M. Kang, Israel Journal of Chemistry 55 (2015) 458–471.
[28] K. Lei, L. Cong, X. Fu, F. Cheng, J. Chen, Inorg. Chem. Front. (2016), doi:http://dx.doi.org/10.1039/c6qi00056h.
[29] T.T. Truong, Y. Liu, Y. Ren, L. Trahey, Y. Sun, ACS Nano 6 (2012) 8067–8077.
[30] T.D. Nyuyen, D. Trong-On, Size and Shape-Controlled Synthesis of Monodisperse Metal Oxide and Mixed Oxide, in: Dr. Yoshitake Masuda (Ed.), Nanocrystals, InTech, 2011, pp. 1–31.
[31] H. Chun Zeng, Current Nanoscience 3 (2007) 177–181.
[32] X. Wang, Y. Li, J. Am. Chem. Soc. 124 (2002) 2880–2881.
[33] K.H. Chang, C.C. Hu, C.Y. Chou, Chem. of Mater. 19 (2007) 2112–2119.
[34] B. Lim, M. Jiang, J. Tao, P.H.C. Camargo, Y. Zhu, Y. Xia, Adv. Func. Mater. 19 (2009) 189–200.
[35] F.S. Gittleson, R.C. Sekol, G. Doubek, M. Linardi, A.D. Taylor, Phys. Chem. Chem. Phys. 16 (2014) 3230–3237.
[36] C.O. Laoire, S. Mukerjee, K.M. Abraham, E.J. Plichta, M.A. Hendrickson, J. Phys. Chem. C 113 (2009) 20127–20134.
[37] C.O. Laoire, S. Mukerjee, K.M. Abraham, E.J. Plichta, M.A. Hendrickson, J. Phys. Chem. C 114 (2010) 9178–9186.